

Aeroacousto-Elastic Modeling for Response Analysis of Helicopter Rotors

Massimo Gennaretti and Giovanni Bernardini

1 Introduction

Helicopter rotors in steady flight are characterized by the generation of vibratory loads and acoustic disturbance. A passenger boarding a helicopter for the first time is undoubtedly struck with the level of vibrations (and noise) that arises within the cabin. It is much higher than that experienced within airplanes and makes helicopter rides significantly less comfortable. The fuselage vibrations caused by the vibratory loads from the main rotor also have a negative impact both on the fatigue-life of the structure and on the functionality of onboard instruments, making their reading difficult, too.

On the other hand, for an external observer, the passage of an helicopter is readily noticed because of the typical tonal noise emitted. It has characteristic frequencies that depend on the performed maneuver and in some flight conditions may produce high levels of acoustic annoyance, insomuch as to make the environmental and public acceptance of helicopters a critical issue.

All this explains why the reduction of both vibratory rotor hub loads and noise emission is one of the most critical (and challenging) goals in the design of new-generation helicopters. In this framework, the availability of reliable simulation tools for the prediction of helicopter rotor noise and vibrations is of primary importance.

The prediction of the vibratory loads transmitted by the main rotor to the fuselage requires the application of an accurate aeroelastic solver derived from coupling a blade structural dynamic model that takes into account both the strong coupling between bending and torsion degrees of freedom and the effect of the significant

M. Gennaretti (✉) · G. Bernardini
University Roma Tre, Via Vasca Navale 79, 00146 Rome, Italy
e-mail: m.gennaretti@uniroma3.it

G. Bernardini
e-mail: g.bernardini@uniroma3.it

deformations usually experienced by slender structures, with an unsteady aerodynamics model that is able to take into account the complex interaction effects arising among the blades. It is a common solution procedure to make the rotor aeroelastic response analysis follow an initial evaluation of the control settings (blade collective and cyclic pitch, shaft angle) through a helicopter trimming process, although a simultaneous evaluation of helicopter trim state and rotor response could be achieved. Once the pressure over the rotor blades is determined from the aeroelastic solver, radiated noise may be computed through a pressure propagation formulation. It is strongly affected by the aerodynamic solution that, therefore, plays a fundamental role both for vibratory loads and acoustic analysis. This is particularly true for the analysis of those flight configurations where blade-vortex interactions, BVI, produce blade impulsive loads and corresponding extremely annoying acoustic effects.

In the last decades, the prediction of helicopter rotor aeroelastic response aimed at examining both emitted noise and vibratory hub loads has been the objective of many researchers operating in the field of rotorcraft. Typically, prediction tools developed to analyze rotor aeroelasticity are based on aerodynamic models that couple 2-D airfoil-theory loads with wake inflow from a 3-D free-wake solver. If blade pressures are needed for aeroacoustic computations, these are usually determined from a different aerodynamic tool that uses blade deformations as an input. An example of this kind of approach is the study aimed to aeroelastic applications presented in Ref. [1], where a multiple-trailer vortex model is used in the free-wake analysis that predicts the wake inflow to be coupled with an aerodynamic load model based on thin airfoil theories. A similar approach is considered in Ref. [2] for aeroacoustic purposes. The combined use of a dual vortex free-wake code with a 2-D aerodynamics code is applied in Refs. [3] and [4] for the aeroelastic and aeroacoustic analysis of rotors aimed to vibration and noise reduction. In Ref. [5] the aerodynamic analysis of rotors in BVI conditions consists of a four-step procedure. An initial rotor trim code based on 2-D aerodynamics is followed by a vortex-lattice free-wake analysis that is then coupled with a roll-up model in order to identify the higher-intensity vortex structures. In turn, these are considered as the interacting vortices in a pressure predictor code based on a 2-D solver. Predictions of vibratory hub loads through an aeroelastic tool combining unsteady 2-D section load models with wake inflow from free-wake analysis are presented in Ref. [6]. An extensive review on tools available for vibratory hub loads prediction is given in Ref. [7].

The aim of this chapter is the presentation of the aeroacousto-elastic simulation tool for helicopter rotors developed in the last years at the Department of Mechanical and Industrial Engineering of University Roma Tre. The models applied for the description of rotor structural dynamics, aerodynamics and aeroacoustics will be outlined in detail, along with the strategy used for their numerical integration. The importance of the role played by the unsteady aerodynamic model in such a kind of solvers will be examined by the numerical investigation. Aeroelastic solvers developed for helicopter and tiltrotor analysis have been presented in Refs. [8–10], the boundary integral equation approach for the velocity potential introduced to predict unsteady aerodynamics of rotors with significant interaction effects (like BVI) has

been described in Ref. [11], while reduced-order aerodynamic models developed for state-space aeroelasticity have been presented in Refs. [12–15]. Applications to rotor aeroacoustic analysis are given in Ref. [16], where the examination of the impact of the aeroelastic modelling on radiated noise prediction is discussed in details.

2 Blade Structural Modeling

A beam-like model is applied to describe the structural dynamics of rotor blades. It is based on the nonlinear bending-torsion formulation presented in Ref. [19] that is valid for straight, slender, homogeneous, isotropic, nonuniform, twisted blades, and undergoing moderate displacements. In this model, second-order terms are retained in the equations after application of an ordering scheme dropping third-order terms (with respect to bending slope) not contributing to damping. The radial displacement is eliminated from the set of equations by solving it in terms of local tension, and thus the resulting structural operator consists of a set of coupled nonlinear differential equations governing the bending of the elastic axis and the blade torsion [20]. Specifically, for $v(x, t)$ denoting the lead-lag bending (lying in the plane of rotation), $w(x, t)$ denoting the flapwise bending, and $\phi(x, t)$ denoting the cross-section torsion about the deformed elastic axis, the blade dynamics is governed by the following set of three dimensionless integro-differential equations [19]:

$$\begin{aligned} & \left[(\Lambda_2 - \Lambda_{21} \sin^2 \theta) v'' \right]'' + \left[\frac{\Lambda_{21}}{2} w'' \sin(2\theta) \right]'' \\ & + \left[\Lambda_{21} (\phi w'' \cos(2\theta) - \phi v'' \sin(2\theta)) \right]'' - [e_A T \cos(\theta + \phi)]'' - (T v')' \\ & = L_v(\mathbf{x}) + p_y(\mathbf{x}) - q_z'(\mathbf{x}) \end{aligned} \quad (1)$$

$$\begin{aligned} & \left[(\Lambda_1 + \Lambda_{21} \sin^2 \theta) w'' \right]'' + \left[\frac{\Lambda_{21}}{2} v'' \sin(2\theta) \right]'' \\ & + \left[\Lambda_{21} (\phi v'' \cos(2\theta) + \phi w'' \sin(2\theta)) \right]'' - [e_A T \sin(\theta + \phi)]'' - (T w')' \\ & = L_w(\mathbf{x}) + p_z(\mathbf{x}) + q_y'(\mathbf{x}) \end{aligned} \quad (2)$$

$$\begin{aligned} & \Lambda_{21} [(w''^2 - v''^2) \sin \theta \cos \theta + v'' w'' \cos(2\theta)] - (\kappa \phi')' - [K^2 T (\phi + \theta)']' \\ & - e_A T (w'' \cos \theta - v'' \sin \theta) \\ & = M_\phi(\mathbf{x}) + q_x(\mathbf{x}) + v' q_y(\mathbf{x}) + w' q_z(\mathbf{x}) \end{aligned} \quad (3)$$

where the tension, T , is given by

$$T = \int_x^1 p_x(\mathbf{x}) d\bar{x} \quad (4)$$

and $()'$ denotes differentiation with respect to the dimensionless spanwise coordinate. In the equations above, dimensionless lengths are related to the blade radius, R ,

while dimensionless time coincides with blade azimuth position. The bending equations (1) and (2) have been obtained by dividing by the factor $m_0 \Omega^2 R$, while the torsion equation (3) is the result of division by the factor $m_0 \Omega^2 R^2$, with m_0 denoting the reference blade mass per unit length, and Ω denoting the angular velocity of the blade. In addition, Λ_1 and Λ_2 are the dimensionless flap and lead-lag bending stiffnesses, respectively, $\Lambda_{21} = \Lambda_2 - \Lambda_1$, κ is the dimensionless torsion rigidity, K is the square of the ratio between the blade cross-section polar radius of gyration and the blade cross-section mass radius of gyration, while e_A denotes the distance between tensile axis and elastic axis [19, 20]. The blade loading terms due to section inertial forces, p_x, p_y, p_z , section inertial moments, q_x, q_y, q_z , and aerodynamic loads per unit length, L_v, L_w, M_ϕ , are functions of the blade section degrees of freedom, $\mathbf{x} = \{v, w, \phi\}$. Note that in (1)–(3) blade precone angle, hinge offset, torque offset, and mass offset, if present, would appear in the description of the distributed inertial and aerodynamic loads.

3 Rotor Aerodynamics Modeling

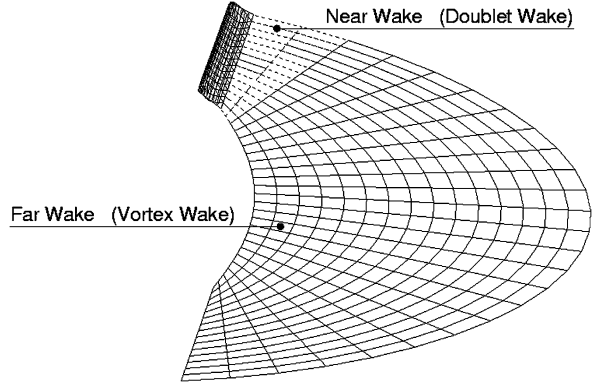
The aerodynamics of helicopters is significantly affected by the interactions among main rotor, fuselage, and tail rotor. However, in many configurations of interest, a crucial role is played by the interactions between rotor blades and rotor wake. These phenomena are known as blade-vortex interactions (BVI) and include blade passages close to the wake, as well as blade-wake impacts that produce impulsive pressures on the blade surface. They strongly contribute to the vibratory loads transmitted to the airframe and generate extremely annoying acoustic effects. Therefore, a simulation tool applied for the optimal design of a new-generation helicopter has to be able to predict BVI occurrence and corresponding aeroelastic and aeroacoustic effects. In view of this, a boundary integral formulation for potential flows suited for the prediction of strong aerodynamic interaction effects has been presented in Ref. [11]. It is a development of the formulation introduced in Ref. [17] and further extended to rotors in forward flight in Ref. [18]. A brief outline of the potential-flow formulation suited for BVI analysis is given in the following.

For the unsteady, incompressible flow around a helicopter rotor, the velocity potential field, φ , may be described through the following boundary integral representation [17, 18]:

$$\varphi(\mathbf{x}, t) = \int_{S_B} \left(G \frac{\partial \varphi}{\partial n} - \varphi \frac{\partial G}{\partial n} \right) dS(\mathbf{y}) - \int_{S_W} \Delta \varphi \frac{\partial G}{\partial n} dS(\mathbf{y}) \quad (5)$$

where S_B and S_W denote blades and wake surfaces, respectively, while $G = -1/4\pi r$ is the unit-source solution of the 3-D Laplace equation, with $r = \|\mathbf{y} - \mathbf{x}\|$. The impermeability boundary condition on S_B yields $\partial \varphi / \partial n = \mathbf{v} \cdot \mathbf{n}$, with \mathbf{v} representing the body velocity and \mathbf{n} its outward unit normal. In addition, $\Delta \varphi$ is the potential jump across the wake surface that is known from the past history of the potential discontinuity at the trailing edge of the corresponding body through the

Fig. 1 Far-wake and near-wake decomposition



Kutta–Joukowski condition, i.e., $\Delta\varphi(\mathbf{x}_W, t) = \Delta\varphi(\mathbf{x}_W^{\text{TE}}, t - \vartheta)$, with $t - \vartheta$ denoting the instant when the wake material point currently in \mathbf{x}_W emanated from the trailing edge point \mathbf{x}_W^{TE} (see Refs. [17] and [18] for details). Equation (5) shows that the potential field is generated by a distribution of sources and doublets over the blades, along with distribution of doublets over the wake surface. However, using the boundary element method for the numerical solution of this equation causes instabilities to arise when wake panels come too close to or impinge on the body surfaces [11]. Thus, this formulation cannot be applied as it is to examine the problem under consideration.

The boundary integral approach proposed in Ref. [11] overcomes this limitation. It introduces the decomposition of the potential field into an incident field, φ_I , and a scattered field, φ_S . The scattered potential is generated by sources and doublets over the body surfaces and by doublets over the wake portion that is very close to the trailing edge from which emanated (near wake, S_W^N). The incident potential is generated by the doublets over the complementary wake region that compose the far wake, S_W^F (see Fig. 1). This is the wake portion that may come in contact with other blades. The scattered potential is discontinuous across S_W^N , whereas the incident potential is discontinuous across S_W^F . Hence, as demonstrated in Ref. [11], for $\varphi = \varphi_I + \varphi_S$, the scattered potential is obtained by

$$\varphi_S(\mathbf{x}, t) = \int_{S_B} \left[G(\chi - \chi_I) - \varphi_S \frac{\partial G}{\partial n} \right] dS(\mathbf{y}) - \int_{S_W^N} \Delta\varphi_S \frac{\partial G}{\partial n} dS(\mathbf{y}) \quad (6)$$

where $\chi = \mathbf{v} \cdot \mathbf{n}$ and $\chi_I = \mathbf{u}_I \cdot \mathbf{n}$, with the velocity induced by the far wake, \mathbf{u}_I , given by

$$\mathbf{u}_I(\mathbf{x}, t) = \nabla\varphi_I(\mathbf{x}, t) = -\nabla \int_{S_W^F} \Delta\varphi_S(\mathbf{y}_W^{\text{TE}}, t - \vartheta) \frac{\partial G}{\partial n} dS(\mathbf{y}) \quad (7)$$

The incident potential affects the scattered potential through the induced-velocity term, χ_I , and, in turn, the scattered potential affects the incident potential by its trailing-edge discontinuity that is convected along the wake and yields the intensity of the doublet distribution over the far wake.

Obtaining the discrete form of (7) by using N panels over the far wake and recalling the vortex-doublet equivalence, the incident velocity field may be evaluated through the following expression:

$$\mathbf{u}_I(\mathbf{x}, t) \approx - \sum_{k=1}^N \Delta\varphi_S(\mathbf{y}_{W_k}^{\text{TE}}, t - \vartheta_k) \int_{C_k} \nabla_{\mathbf{x}} G \times d\mathbf{y} \quad (8)$$

where C_k denotes the contour line of the k th far wake panel, $\mathbf{y}_{W_k}^{\text{TE}}$ is the trailing edge position where the wake material point currently in \mathbf{y}_{W_k} emanated at time $t - \vartheta_k$, and $\nabla_{\mathbf{x}}$ denotes gradient operator with respect to the variable \mathbf{x} . This equation represents the velocity field given by the Biot–Savart law applied to the vortices having the shape of the far wake panel contours and intensity $\Delta\varphi_S(\mathbf{y}_{W_k}^{\text{TE}}, t - \vartheta_k)$. Equation (8) is applied to evaluate both the term χ_I in (6) and, once extended to the whole wake, the velocity field in the free-wake distortion analysis, if required.

The final step of the formulation consists of introducing in (8) a finite-thickness vortex model that assures a regular distribution of the induced velocity within the vortex core, and thus a stable and regular solution even in body-vortex impact conditions [11]. The description of the wake influence through the use of finite-core vortices is a way to include also diffusivity and vortex-stretching effects that, otherwise, would not be taken into account in a potential-flow aerodynamic formulation (see Refs. [21] and [22] for details on this issue).

Equation (6) is solved numerically by boundary elements, i.e., by dividing S_B and S_W^N into quadrilateral panels, assuming φ_S , χ , χ_I , and $\Delta\varphi_S$ to be piecewise constant (zeroth-order boundary element method, BEM) and imposing that the equation be satisfied at the center of each body element (collocation method) [11].

Once the potential field is known, the Bernoulli theorem yields the pressure distribution (see Appendix A), and hence blade loads may be evaluated through integration.

3.1 Aerodynamic Loads From Airfoil Theories

In several aeroelastic prediction tools commonly used in rotorcraft applications, the blade aerodynamic forcing terms are obtained as radial integration of the loads given by sectional aerodynamics models. These are typically derived from airfoil unsteady aerodynamics theories, corrected with wake inflow to take into account the three-dimensional effects due to wake vortices.

For a thin, straight airfoil moving in an incompressible flow, following the Greenberg theory [23] (which is the extension of the Theodorsen theory [24] to pulsating airstream), it is possible to determine the aerodynamic force acting on it by combining the noncirculatory lift, L_{nc} , orthogonal to the chord with the circulatory lift, L_c , directed along the normal to the relative wind (see, for instance, Ref. [20]). Specifically, for ρ denoting the air density and b denoting the airfoil semi-chord length,

the noncirculatory lift is expressed as

$$L_{nc}(t) = \pi \rho b^2 \dot{v}_{1/2}^n \quad (9)$$

where $\dot{v}_{1/2}^n$ denotes the time derivative of the normal component of the relative wind evaluated at the airfoil mid point (positive upwards). The circulatory lift, which in practical applications is the most relevant load contribution, is given by the expression

$$L_c(t) = 2\pi \rho b V \mathcal{F}^{-1}[C(k)\tilde{v}_{3/4}^n] \quad (10)$$

where V denotes the relative wind velocity, \mathcal{F} denotes Fourier transformation, and $\tilde{v}_{3/4}^n = \mathcal{F}(v_{3/4}^n)$ with $v_{3/4}^n$ representing the normal component of the relative wind evaluated at the airfoil 3/4-chord point. In addition, $C(k)$ is the lift deficiency (complex) function defined by Theodorsen [24] in terms of the reduced frequency, $k = \omega b / \bar{V}$, where ω is the variable in the Fourier domain, and \bar{V} is the mean (or reference) value of V which is responsible for the shed vorticity convection (see Ref. [25] for a detailed analysis of the effects of nonuniform convection of the shed vorticity along the wake). For a harmonic $v_{3/4}^n$ input, $C(k)$ defines gain and phase shift of the L_c/V harmonic response. The set of the aerodynamic loads acting on the airfoil includes also the pitching moment about the 1/4-chord point (positive clockwise for the relative wind directed from left to right), which is given by [23]

$$M_{1/4}(t) = -\frac{b}{2}L_{nc} - \pi\rho\frac{b^3}{2}\left(V\omega_a + \frac{b}{4}\dot{\omega}_a\right) \quad (11)$$

where ω_a is the angular velocity of the airfoil. Once $v_{1/2}^n$, $v_{3/4}^n$, ω_a , and V are expressed in terms of the blade degrees of freedom (a major elastic contribution from blade lag may appear also in V), Eqs. (9), (10), and (11), combined with a model to take into account drag effects, may be applied to develop an aeroelastic formulation for helicopter rotors. Note that a similar unsteady aerodynamics formulation has been developed by Loewy for the airfoil of a rotor blade in hovering or axial flow [26].

Some difficulties in the application of unsteady aerodynamics airfoil theories stem from the presence of the lift deficiency function. Indeed, it is a transcendental function of the reduced frequency and hence requires the introduction of a convolution integral for the evaluation of the circulatory lift (see (10)). Alternatively, it may be expressed through a Padé approximant (see, for instance, Ref. [27]), thus avoiding the computation of convolution integrals, at the cost of introducing some aerodynamic states in the state-space realization of the aeroelastic problem. However, this problem does not appear when the so-called quasi-steady approximation of the airfoil theory is applied. It consists of assuming that very low frequencies are involved in the aeroelastic process and observing that $C(k) \rightarrow 1$ as $k \rightarrow 0$. In this case the transcendent terms in the circulatory lift disappear, and the model is considerably simplified. In many research and industry applications, the inaccuracies introduced by the quasi-steady aerodynamic model are compensated by coupling it with dynamic wake inflow models taking into account the influence of shed and

trailed vorticity coming also from aeroelastic effects. Widely used dynamic wake inflow models are those introduced by Peters and his coworkers (see, for instance, Refs. [28–30]). When the wake inflow is evaluated without considering aeroelastic effects (i.e., it is assumed to be independent of the blade degrees of freedom), it is referred to as static inflow; coupled with the quasi-steady approximation of the airfoil theory, it yields a simplified but user-friendly aerodynamic model yet frequently applied in rotorcraft solvers.

Finally, note that for the analysis of helicopter rotors operating at high forward flight speeds, the unsteady aerodynamics modeling has to take into account also the effects of the reverse flow occurring at the blade root region in the retreating side, along with the influence of the phenomenon of dynamic stall caused by the onset of large torsional airloads and vibrations on the blade [22].

4 Harmonic Balance for Aeroelastic Response Analysis

Equations (1), (2), and (3) governing the blade structural dynamics coupled with the unsteady aerodynamic load modelling yield the aeroelastic integro-differential equations to be integrated. Here, the space integration is performed through the Galerkin approach, starting from the following description of the elastic axis deformation as a linear combination of shape functions

$$\begin{aligned} v(x, t) &= \sum_n q_n^v(t) \Psi_n^v(x); & w(x, t) &= \sum_n q_n^w(t) \Psi_n^w(x); \\ \phi(x, t) &= \sum_n q_n^\phi(t) \Psi_n^\phi(x) \end{aligned}$$

For instance, considering a hingeless rotor, Ψ_n^v , Ψ_n^w , and Ψ_n^ϕ , might conveniently be chosen as the bending and torsion natural modes of vibration of a nonrotating cantilever beam [20]. The resulting aeroelastic system consists of a set of nonlinear ordinary differential equations of the type

$$\mathbf{M}(t)\ddot{\mathbf{q}} + \mathbf{C}(t)\dot{\mathbf{q}} + \mathbf{K}(t)\mathbf{q} = \mathbf{f}_{\text{str}}^{\text{nl}}(t, \mathbf{q}) + \mathbf{f}_{\text{aer}}(t, \mathbf{q}) \quad (12)$$

where \mathbf{q} denotes the vector of the Lagrangian coordinates, whereas \mathbf{M} , \mathbf{C} , and \mathbf{K} are time-periodic, mass, damping, and stiffness structural matrices representing the linear structural terms (note that these matrices are time-variant because of the cyclic pitch contribution). Nonlinear structural contributions are collected in the forcing vector $\mathbf{f}_{\text{str}}^{\text{nl}}(t, \mathbf{q})$, whereas vector $\mathbf{f}_{\text{aer}}(t, \mathbf{q})$ collects the generalized aerodynamic forces. Specifically, the generalized forces related to lead-lag, flap, and torsion equations are, respectively, given by

$$f_{\text{aer}_j}^v = \int_{x_R}^1 L_v \Psi_j^v dx; \quad f_{\text{aer}_j}^w = \int_{x_R}^1 L_w \Psi_j^w dx; \quad f_{\text{aer}_j}^\phi = \int_{x_R}^1 M_\phi \Psi_j^\phi dx$$

where x_R is the dimensionless aerodynamic root cutout, while L_v , L_w , and M_ϕ denote, respectively, sectional force components along the bending directions and sectional torsion moment about the elastic axis. Sectional aerodynamic loads may be obtained either by integration along the airfoil contour of the pressure distribution given by the BEM solver outlined above (or any other CFD tool available) or by using the expressions in (9)–(11) derived from the airfoil theory.

Since the aim is the prediction of the aeroelastic and aeroacoustic steady periodic response during forward flight, the aeroelastic system in (12) is solved by using the harmonic balance approach. It is a methodology suitable for the analysis of the asymptotic solution (as time goes to infinity) of differential equations forced by periodic terms, as in the present case. The harmonic balance solution consists of: (i) express LHS and RHS of the aeroelastic system (Eq. (12)) in terms of their Fourier series; (ii) equate the resulting coefficients; and (iii) solve the corresponding algebraic system in terms of the unknown Fourier coefficients of the Lagrangian coordinates of the problem. Specifically, expressing \mathbf{q} and $\mathbf{f} = \mathbf{f}_{\text{str}}^{\text{nl}} + \mathbf{f}_{\text{aer}}$ in terms of the Fourier series

$$\begin{aligned}\mathbf{q}(t) &= \mathbf{q}_0 + \sum_{n=1}^N [\mathbf{q}_n^c \cos(\Omega_n t) + \mathbf{q}_n^s \sin(\Omega_n t)] \\ \mathbf{f}(t) &= \mathbf{f}_0 + \sum_{n=1}^N [\mathbf{f}_n^c \cos(\Omega_n t) + \mathbf{f}_n^s \sin(\Omega_n t)]\end{aligned}$$

(where \mathbf{q}_n^c , \mathbf{q}_n^s , \mathbf{f}_n^c , and \mathbf{f}_n^s denote the cosine and sine components of the n th harmonic of \mathbf{q} and \mathbf{f} , whereas $\Omega_n = n\Omega$ with Ω representing the fundamental frequency, i.e., the rotor angular velocity) and then combining with (12) yields the following representation of the aeroelastic system harmonic components:

$$[\hat{\mathbf{M}} + \hat{\mathbf{C}} + \hat{\mathbf{K}}]\hat{\mathbf{q}} = \hat{\mathbf{f}} \quad (13)$$

where $\hat{\mathbf{q}}^T = \{\mathbf{q}_0^T \ \mathbf{q}_1^{cT} \ \mathbf{q}_1^{sT} \ \mathbf{q}_2^{cT} \ \mathbf{q}_2^{sT} \ \dots\}$ and $\hat{\mathbf{f}}^T = \{\mathbf{f}_0^T \ \mathbf{f}_1^{cT} \ \mathbf{f}_1^{sT} \ \mathbf{f}_2^{cT} \ \mathbf{f}_2^{sT} \ \dots\}$. The matrices $\hat{\mathbf{M}}$, $\hat{\mathbf{C}}$, and $\hat{\mathbf{K}}$ in (13) come out from (12) by combining the harmonics of the \mathbf{q} , $\dot{\mathbf{q}}$, and $\ddot{\mathbf{q}}$ terms with the harmonics of the matrices \mathbf{M} , \mathbf{C} , and \mathbf{K} . In particular, if \mathbf{M} , \mathbf{C} , and \mathbf{K} were constant matrices, in (13) one would have block-diagonal matrices, and each harmonic of \mathbf{q} would depend only on the same harmonic of \mathbf{f} (the \mathbf{q} -harmonics equations would be uncoupled). Instead, in the problem under examination the structural matrices are periodic, and hence, once expressed in terms of the Fourier series and combined with the harmonics of \mathbf{q} , $\dot{\mathbf{q}}$, and $\ddot{\mathbf{q}}$, they yield fully populated $\hat{\mathbf{M}}$, $\hat{\mathbf{C}}$, and $\hat{\mathbf{K}}$ matrices, thus coupling the algebraic equations for the unknown harmonics in $\hat{\mathbf{q}}$ (as an example, in Appendix B the $\hat{\mathbf{K}}$ matrix is given in terms of the harmonics of \mathbf{K}).

Because of the presence of nonlinear structural terms and of aerodynamic contributions in $\hat{\mathbf{f}}$, (13) has to be solved using an iterative procedure. To this aim, the Newton–Raphson method with a simplified Jacobian matrix is applied. Specifically,

the harmonic aeroelastic solution is obtained from convergence of the following iterative procedure (with n indicating the iteration step number):

$$\hat{\mathbf{q}}_n = [\hat{\mathbf{M}} + \hat{\mathbf{C}} + \hat{\mathbf{K}} - \hat{\mathbf{J}}_{\text{aer}}]^{-1} [\hat{\mathbf{f}}_{n-1} - \hat{\mathbf{J}}_{\text{aer}} \hat{\mathbf{q}}_{n-1}] \quad (14)$$

where $\hat{\mathbf{J}}_{\text{aer}}$ is the aerodynamic Jacobian evaluated at $\hat{\mathbf{q}} = \mathbf{0}$, while $\hat{\mathbf{f}}_{n-1}$ denotes the nonlinear structural terms and aerodynamic loads evaluated at $\hat{\mathbf{q}} = \hat{\mathbf{q}}_{n-1}$ (i.e., through the Lagrangian coordinates given by the previous iteration step). Under this assumption, the aerodynamic portion of the forcing term is equivalent to $\hat{\mathbf{f}}_{\text{aer}}^0 + \hat{\mathbf{f}}_{\text{aer}}^{\text{nl}}$, with $\hat{\mathbf{f}}_{\text{aer}}^0$ denoting the aerodynamic load portion that is not influenced by the structural deformation. The introduced approximation of the Jacobian is convenient in that it implies that the matrix inversion required in (14) has to be evaluated only one time. If convergence problems arise (because of large differences between the local aerodynamic gradient and $\hat{\mathbf{J}}_{\text{aer}}$), the aerodynamic Jacobian has to be re-evaluated during the iteration process (either analytically or numerically, depending on the aerodynamic solver applied), along with the inverted global Jacobian matrix.

5 Radiated Noise Modeling

Once the aeroelastic (and hence aerodynamic) response has been determined, it is possible to proceed with the evaluation of the noise radiated by the helicopter rotor. Indeed, it requires the knowledge of blade motion, blade surface pressure distribution, and, for transonic configurations, also the flow field around it. The aeroacoustic solver applied in the prediction tool developed by the authors is based on the well-known Ffowcs Williams–Hawkings equation, written for compressible flows undergoing transformations with negligible entropy changes [31]. In this case, the pressure-density relationship is approximated by the linear term of its series expansion, namely $p' = c_0^2 \tilde{\rho}$, where p' denotes the acoustic pressure disturbance, c_0 is the speed of sound in the undisturbed medium, and $\tilde{\rho}$ denotes the density perturbation.

The Ffowcs Williams–Hawkings equation represents a rearrangement of the mass and momentum conservation laws into an inhomogeneous wave equation which extends to the presence of moving bodies the field of application of the Lighthill theory for the aerodynamically generated sound. In its more general form, for $f(\mathbf{x}, t) = 0$ describing an arbitrary moving surface, the Ffowcs Williams–Hawkings equation reads

$$\begin{aligned} & \frac{1}{c_0^2} \frac{\partial^2 p'}{\partial t^2} - \bar{\nabla}^2 p' \\ &= \frac{\bar{\partial}}{\partial t} \{ [\rho_0 v_n + \rho(u_n - v_n)] \delta(f) \} \\ & \quad - \frac{\bar{\partial}}{\partial x_i} \{ [\Delta P_{ij} n_j + \rho u_i(u_n - v_n)] \delta(f) \} + \frac{\bar{\partial}^2}{\partial x_i \partial x_j} \{ T_{ij} H(f) \} \end{aligned} \quad (15)$$

where $T_{ij} = \rho u_i u_j + P_{ij} - c_0^2 \tilde{\rho} \delta_{ij}$ denotes a component of the Lighthill tensor, P_{ij} is a component of the compressive stress tensor, $\Delta P_{ij} = P_{ij} - p_0 \delta_{ij}$ with δ_{ij} representing the Kronecker delta function, while p_0 is the pressure of the undisturbed medium. In addition, the overbar denotes generalized derivative, the fluid and body velocity components are indicated by u_i and v_i , respectively, whereas the subscript n denotes projection along the outward normal to the surface $f(\mathbf{x}, t) = 0$. The Dirac and Heaviside functions on the right-hand side point out the particular nature of the different source terms: two surface terms directly related to the effects of the discontinuity $f(\mathbf{x}, t) = 0$ in the flow field and a volume term accounting for all sources acting outside $f(\mathbf{x}, t) = 0$. Generally, $f(\mathbf{x}, t) = 0$ coincides with the body surface, S_B , so that the impermeability condition $u_n = v_n$ notably simplifies (15). Furthermore, the assumptions of an inviscid flow reduces the compressive stress tensor to the scalar pressure field upon the surface, i.e., $\Delta P_{ij} = (p - p_0) \delta_{ij} = \tilde{p} \delta_{ij}$.

The use of the standard Green function approach yields the solution of (15) in terms of a boundary integral form, suitable for numerical purposes. Specifically, the aeroacoustic computational tool is based on the widely used boundary integral representation known as formulation 1A, developed by Farassat [32, 33]. Note that the presence of three different terms in (15) gives rise to three separate integral contributions known as thickness, loading, and quadrupole noise, each related to a well-defined generating noise mechanism. The thickness terms only depends on the blade geometry and the kinematics of the problem, the loading term is related to the blade airload, whereas the quadrupole source contribution accounts for the possible nonlinear effects taking place in the flow field. Generally, this last term can be reasonably neglected, provided that the blade rotational velocity is far from the transonic/supersonic range. Within formulation 1A, the thickness and loading integral terms (identified as p'_T and p'_L , respectively) assume the following forms:

$$\begin{aligned}
 4\pi p'_T(\mathbf{x}, t) &= \int_{S_B} \left[\frac{\rho_0 \dot{v}_n}{r|1 - M_r|^2} \right]_\tau dS(\mathbf{y}) \\
 &\quad + \int_{S_B} \left[\frac{\rho_0 v_n (r \dot{M}_i \hat{r}_i + c_0 M_r - c_0 M^2)}{r^2 |1 - M_r|^3} \right]_\tau dS(\mathbf{y}) \\
 4\pi p'_L(\mathbf{x}, t) &= \frac{1}{c_0} \int_{S_B} \left[\frac{\tilde{p} n_i \hat{r}_i + \tilde{p} \dot{n}_i \hat{r}_i}{r|1 - M_r|^2} \right]_\tau dS(\mathbf{y}) + \int_{S_B} \left[\frac{\tilde{p} n_i \hat{r}_i - \tilde{p} M_n}{r^2 |1 - M_r|^2} \right]_\tau dS(\mathbf{y}) \\
 &\quad + \frac{1}{c_0} \int_{S_B} \left[\frac{\tilde{p} n_i \hat{r}_i}{r^2 |1 - M_r|^3} (r \dot{M}_i \hat{r}_i + c_0 M_r - c_0 M^2) \right]_\tau dS(\mathbf{y})
 \end{aligned}$$

with \mathbf{r} denoting the distance between \mathbf{x} and \mathbf{y} , $r = |\mathbf{r}|$, and $\hat{\mathbf{r}} = \mathbf{r}/r$. In addition, $\mathbf{M} = \mathbf{v}/c_0$ is the local Mach vector, $M = |\mathbf{M}|$, and $M_r = \mathbf{M} \cdot \hat{\mathbf{r}}$.

Formulation 1A is classified as a retarded-time formulation, since it requires retarded functions to be integrated over a domain corresponding to the actual rotor blade surface [32, 33]. The integrals are computed through a simple zeroth-order formulation applied to the blade surface discretized through panels, where the integral kernels are assumed to be uniform and equal to the values at the centroids.

The notation $[\dots]_\tau$ indicates that these quantities must be evaluated at the emission time τ . Indeed, a backward-in-time integration scheme is adopted, by fixing the observer time t and computing the corresponding emission time τ at each source point by solving the root-finding problem for the equation

$$\tau - t + \frac{r}{c_0} = \tau - t + \frac{|\mathbf{x}(t) - \mathbf{y}(\tau)|}{c_0} = 0$$

For given observer time t and location \mathbf{x} , τ represents the instant when the contribution to the noise signature was released from \mathbf{y} . Due to the rotational blade motion, the root-searching scheme requires an iterative process. Nonetheless, the overall computational effort of the integration procedure is quite limited (even for very fine meshes), and the acoustic pressure time history can be achieved at each point in a handful of seconds. The availability of the noise signature in time domain enables the evaluation of the corresponding spectrum in the frequency domain (via a discrete Fourier transform) and the noise level in dB. Thus, by accounting for a prescribed map of observer locations, it is possible to draw the noise level contour plot and to appreciate the main features of the acoustic pressure field, both in terms of noise level and directivity.

6 Numerical Investigation on Aeroelastic and Aeroacoustic Responses

Here, some results from the aeroelastic/aeroacoustic formulation for helicopter rotors outlined above are presented. First, a short overview of the validation analysis of the aeroelastic solver carried out in the past is illustrated, along with an examination of the impact of the aerodynamic modeling on the simulation of helicopter rotor aeroelastic response. Then, some correlations of aeroacoustic predictions with experimental measurements are shown.

6.1 Aeroelastic Responses

First, the validation analysis concerning the rotor model examined in Ref. [34] is considered. It is a four-bladed rotor with radius $R = 4.93$ m, constant chord $c = 0.395$ m, NACA 0012 section profile, and a linear twist angle of -8° . The sectional rotor structural properties considered in the analysis are $\Lambda_1 = 0.008345$, $\Lambda_2 = 0.023198$, $\kappa = 0.00225$, and blade mass per unit length $m = 6.462$ kg/m (see Ref. [34] for additional details). The rotor has been examined in level flight conditions with rotational speed $\Omega = 40$ rad/s, at advance ratios $\mu = 0.15$ and $\mu = 0.3$. For the two advance ratios investigated, rotor shaft angles, and collective and cyclic pitch angles of the blades considered are those determined in Ref. [34] with linear inflow trimming.

Fig. 2 Blade tip deformation for $\mu = 0.15$

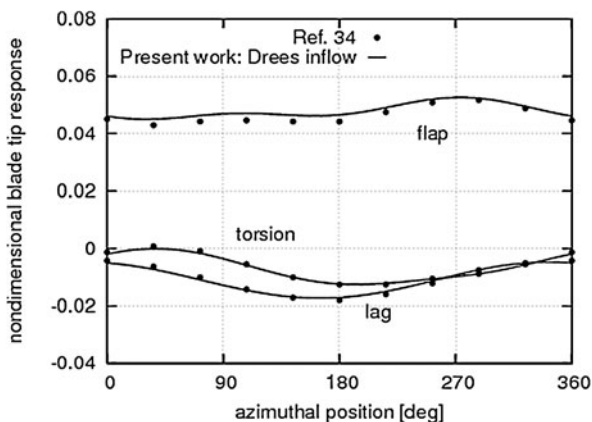
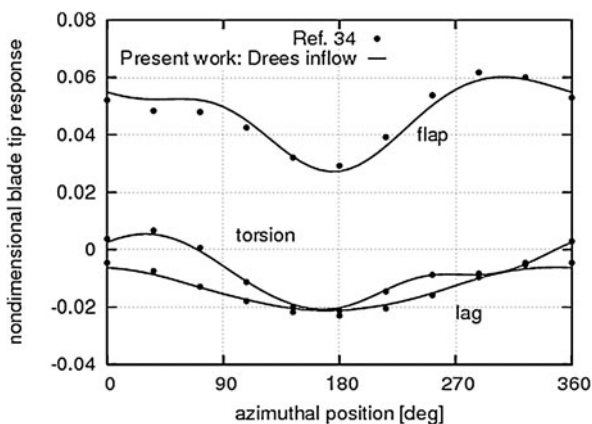


Fig. 3 Blade tip deformation for $\mu = 0.30$



Some results from the aeroelastic formulation presented here are compared with those given in Ref. [34], based on the rotor code UMARC [35] that is a well-known, widely used aeroelastic solver. It uses a nonlinear, finite-element approach for the structural analysis, whereas unsteady aerodynamic loads are given by combination of 2-D airfoil theory with wake inflow obtained either from analytical models or from free-wake analysis [6, 35]. In this case, in order to describe the aerodynamic loads similarly to Ref. [34], the sectional quasi-steady aerodynamic theory with linear Drees wake inflow is applied (see also Ref. [8]). Figures 2 and 3 show that, for both advance ratios, the blade tip deformations (namely, lag, flap, and torsion) predicted by the present formulation are in good agreement with those presented in Ref. [34]. The same level of agreement is shown in Fig. 4 in which, for $\mu = 0.3$, the comparison is presented in terms of the 4/rev vibrating loads calculated at the rotor hub (it is worth noting that the hub is forced by the combination of the loads transmitted by each rotor blade, and the harmonics of the resulting loads are multiples of the number of the rotor blades).

Fig. 4 4/rev hub loads for $\mu = 0.30$

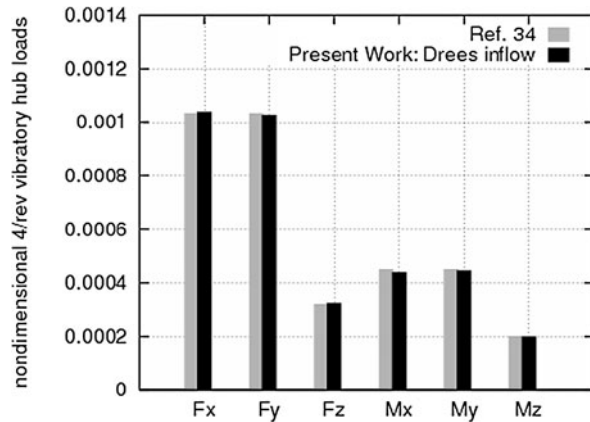
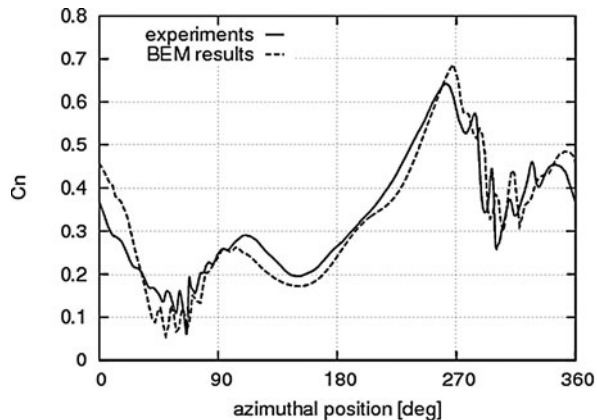


Fig. 5 C_n at blade section $r/R = 0.92$



Next, some results which concern the validation of the BEM solver outlined in Sect. 3 are shown. These have already been presented in Ref. [8] and correlate numerical predictions from the BEM tool with experimental results obtained within the European Project HELISHAPE [36]. The rotor considered is the four-bladed EC/ONERA 7A main rotor, tested at the DNW wind tunnel [36]. It has rectangular blades with aspect ratio equal to 15 and is examined in 6° -descent forward flight condition, with rotational speed $\Omega = 101$ rad/s, advance ratio $\mu = 0.166$, and rotational tip Mach number $M_\Omega = 0.615$ (related to HELISHAPE Datapoint 70). Figures 5 and 6 show the comparisons between measurements and free-wake BEM predictions in terms of the normal force coefficient, C_n , respectively at blade sections $r/R = 0.92$ and $r/R = 0.98$. These results demonstrate that the presented BEM solver has a good capability of predicting unsteady airloads, with inclusion of BVI effects that are well captured in terms of both oscillation amplitude and azimuth location occurrence.

Now, the assessment of the effects of the aerodynamic model on the aeroelastic response simulation is analyzed. Specifically, the attention is focused on the

Fig. 6 C_n at blade section
 $r/R = 0.98$

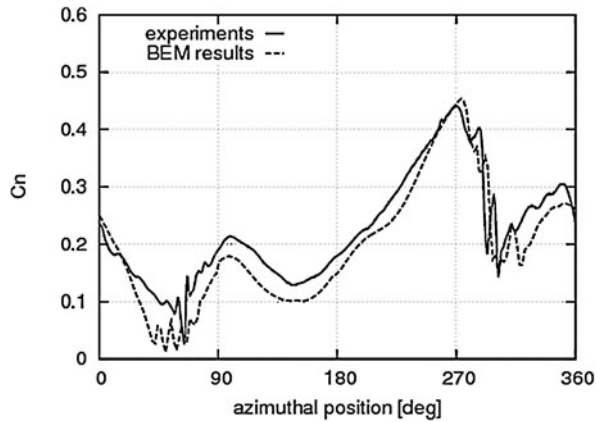
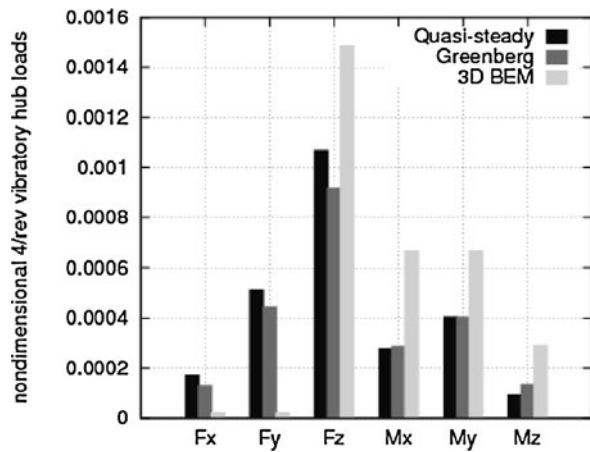


Fig. 7 4/rev hub loads for
 $\mu = 0.15$



prediction of the vibratory loads arising at the hub of the model rotor described in Ref. [34]. These have been carried out through: (i) sectional quasi-steady aerodynamics with wake inflow from the BEM solver with a prescribed wake shape, (ii) sectional unsteady aerodynamics (Greenberg's theory) with wake inflow from the BEM solver with a prescribed wake shape, and (iii) unsteady aerodynamic loads given directly from the 3-D BEM potential formulation with a prescribed wake shape. In these analyses, the prescribed wake consists of the surface swept by the trailing edges of the blades during their motion. Note that, using the expression in Eq. (8), the wake effect is equivalent to that of a vortex-lattice with the presence of both trailed and shed vortices: the effects of shed vorticity is not taken into account in the evaluation of the wake inflow used in Greenberg's theory.

For advance ratio $\mu = 0.15$, Fig. 7 depicts the comparison among the results from the three aerodynamic models considered in terms of vibratory hub loads, while the results for $\mu = 0.30$ are given in Fig. 8. These results demonstrate that, at least for the prediction of the vibratory hub loads, the aerodynamic quasi-steady approxima-

Fig. 8 4/rev hub loads for $\mu = 0.30$

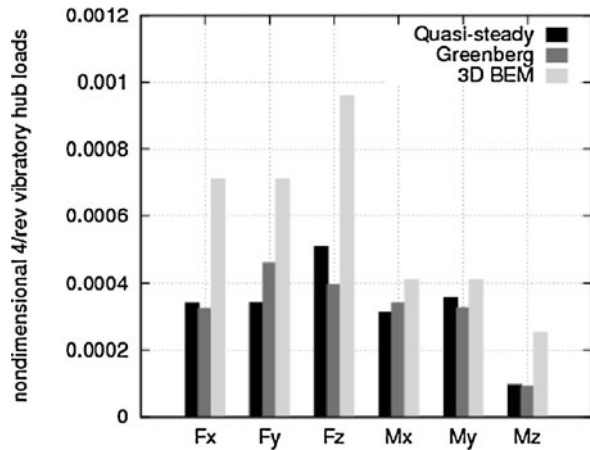
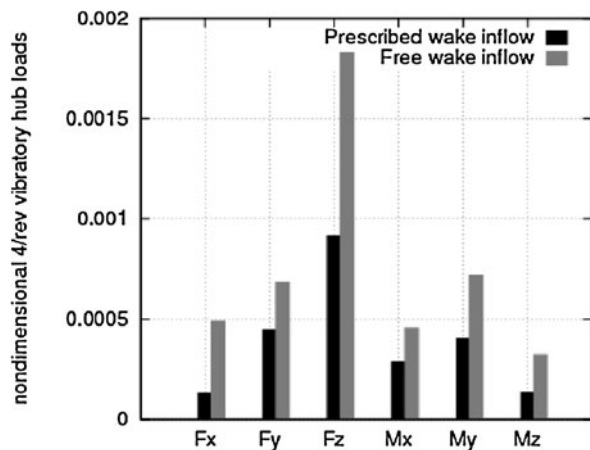


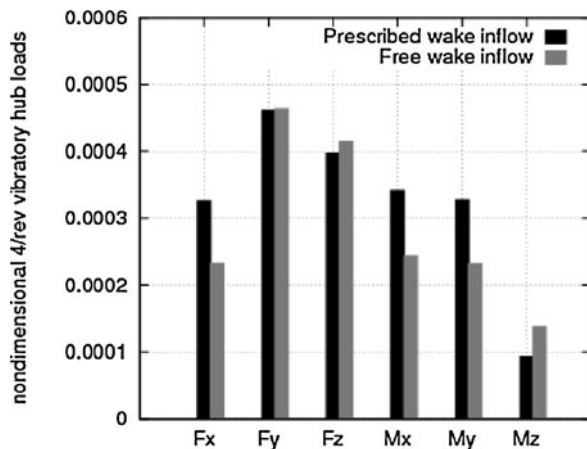
Fig. 9 4/rev hub loads for $\mu = 0.15$



tion combined with wake inflow from a 3-D solver gives results that are comparable with those from the application of the complete unsteady section theory (i.e., with inclusion of lift deficiency function effects). Rather, different results come from the evaluation of loads directly through the BEM solver, thus proving the relevant contribution due to 3-D and interaction effects.

Finally, fixing the sectional Greenberg aerodynamic model, Figs. 9 and 10 show the influence of the wake inflow model applied on the predicted hub loads. While for $\mu = 0.30$, wake inflows from prescribed wake shape and from free-wake analysis give different but comparable hub loads, for $\mu = 0.15$, they yield dramatically different hub loads predictions. This is due to the fact that the role of the wake is crucial when the wake remains in the vicinity of the rotor ($\mu = 0.15$ case), whereas it tends to decrease as the wake rapidly goes far from the rotor ($\mu = 0.30$ case). This confirms the great attention that has to be paid on the definition of the wake contribution in helicopter rotor aeroelastic analyses.

Fig. 10 4/rev hub loads for $\mu = 0.30$



6.2 Aeroacoustic Responses

Here, the present formulation is applied to the aeroacoustic analysis helicopter rotors in BVI conditions. The rotor considered is the above-mentioned four-bladed EC/ONERA 7A main rotor analyzed within the European Project HELISHAPE [36], and the flight condition examined is the 6°-descent forward flight (HELISHAPE Datapoint 70). The results discussed in the following have already been presented by the authors in Ref. [11]. The numerical analysis has been performed using the azimuthal step $\Delta\psi = 1.33^\circ$ and including two wake spirals. In BVI conditions the aerodynamic field and the corresponding radiated noise are strongly dependent on the shape of the wake and on its distance from the rotor blades, and thus an accurate prediction of the distorted wake is essential. Figures 11 and 12 depict rear and side view, respectively, of the distorted wake geometry given by the present free-wake analysis. These figures show clearly that during the descent flight the wake remains close to the rotor disk, thus inducing severe blade/wake impingement. In addition, for the sake of clarity, Fig. 13 depicts the wake of only one blade and shows the impact between one rotor blade and the wake generated by the preceding blade. This figure concerns the azimuth position $\psi = 65^\circ$ and indicates that the strongest BVI occurs at positions around $\psi = 60^\circ$ in the advancing side, although close blade/wake interaction occurs also around $\psi = 310^\circ$ in the retreating side. For this flight condition, the experimental measurements have detected strong BVI occurrence at azimuth positions around $\psi = 55^\circ$ [36].

Once the blade pressure distribution has been obtained from the aeroelastic solver, the aeroacoustic formulation described in Sect. 5 has been applied to predict the noise emitted by the helicopter rotor. Figures 14, 15 and 16 present a comparison between the measured acoustic pressure and the acoustic time signature given by the numerical predictions concerning observers that are located 2.286 m below the rotor disk. The first one (Obs A) corresponds to the upstream microphone that is 2-m distant from the rotor hub (advancing rotor side), the second one (Obs B) corresponds to the upstream microphone located 3 m far from the rotor hub (advancing rotor

Fig. 11 Rotor 7A: rear view of computed wake geometry

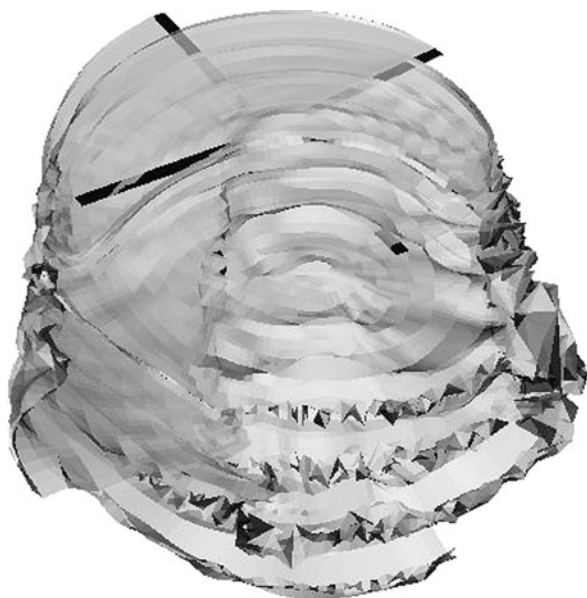


Fig. 12 Rotor 7A: side view of computed wake geometry

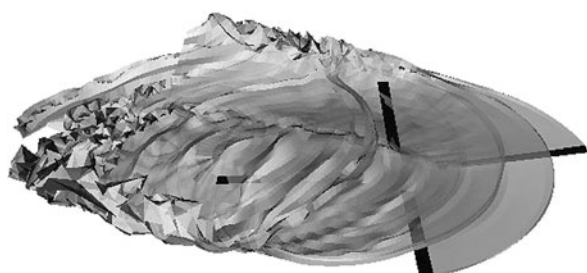


Fig. 13 Rotor 7A: blade/wake impingement

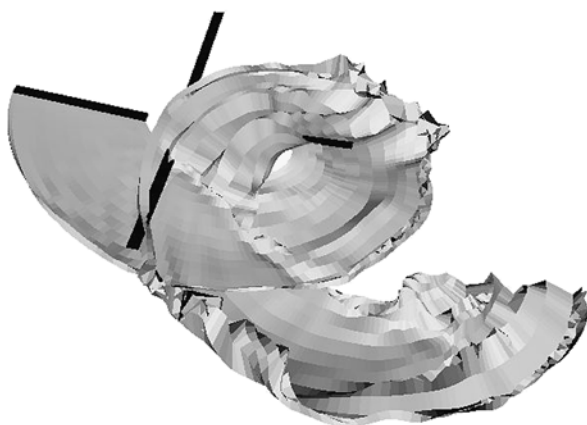
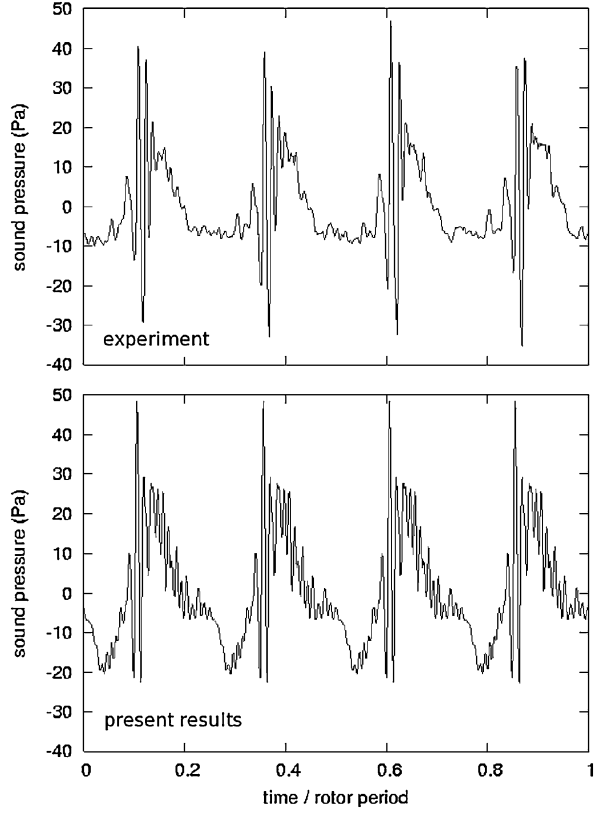


Fig. 14 Rotor 7A:
experimental and numerical
acoustic signature at Obs A



side), while the third one (Obs C) corresponds to the upstream microphone located 3.5 m far from the rotor hub (retreating rotor side). The acoustic correlations show that, although the numerical results present a bit more oscillating behavior with respect to the experimental data, the impulsiveness of the signal and the intensity of the peaks due to BVI are well captured by the aeroacousto-elastic solvers outlined here that, therefore, seem to be suitable tools for helicopter design applications.

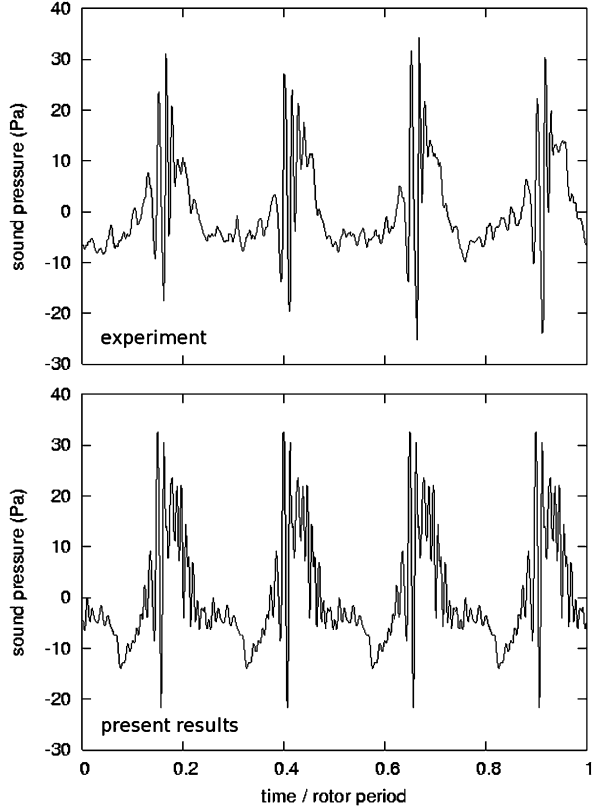
Appendix A

From the decomposition of the potential field into a scattered component, φ_S , and an incident component, φ_I , introduced in Sect. 3, in a body-fixed frame of reference the Bernoulli theorem reads

$$\dot{\varphi}_S + \dot{\varphi}_I - \mathbf{v}_B \cdot (\nabla \varphi_S + \mathbf{u}_I) + \frac{\|\nabla \varphi_S + \mathbf{u}_I\|^2}{2} + \frac{p}{\rho} = \frac{p_0}{\rho} \quad (\text{A.1})$$

where p_0 is the pressure of the undisturbed medium. In order to evaluate the pressure distribution, the expression above requires the determination of $\dot{\varphi}_I$, which is the only

Fig. 15 Rotor 7A:
experimental and numerical
acoustic signature at Obs B



term not directly available from the aerodynamic formulation presented in Sect. 3. The incident potential (and the corresponding time derivative) could be obtained from the doublet distribution over the far wake, S_W^F , using the following integral expression (see also Eq. (7)):

$$\varphi_I(\mathbf{x}, t) = - \int_{S_W^F} \Delta\varphi_S(\mathbf{y}_W^{\text{TE}}, t - \vartheta) \frac{\partial G}{\partial n} dS(\mathbf{y}) \quad (\text{A.2})$$

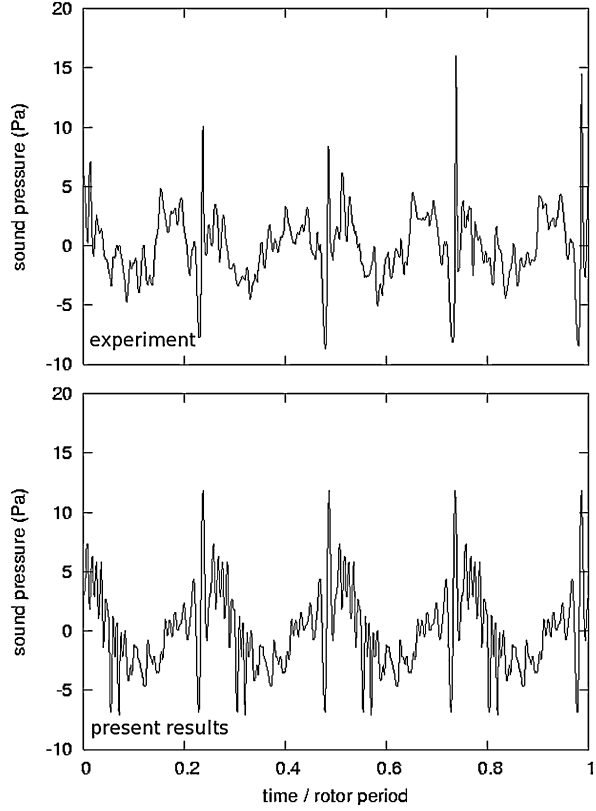
that, dividing the wake into panels, $S_{W_k}^F$, is approximated as

$$\varphi_I(\mathbf{x}, t) \approx - \sum_{k=1}^N -\Delta\varphi_S(\mathbf{y}_{W_k}^{\text{TE}}, t - \vartheta_k) \int_{S_{W_k}^F} \frac{\partial G}{\partial n} dS(\mathbf{y}) \quad (\text{A.3})$$

However, as already mentioned in Sect. 3, the above expression cannot be applied to those wake panels coming in contact with the body or passing very close to it (BVI occurrence), in that they become numerically unstable and yield unrealistic potential distributions.

In order to avoid this problem, for the far wake panels, the contribution to $\dot{\varphi}_I$ is obtained in the following robust and accurate way. Consider the closed vortex at

Fig. 16 Rotor 7A:
experimental and numerical
acoustic signature at Obs C



the contour of the k th panel of the far wake that might risk to come in contact with the body, $C_k = \partial S_{W_k}^F$, and introduce a frame of reference rigidly connected with it such that, under the assumption of undeformed wake panel, the incident potential induced by the vortex is constant in time on each point of it. Next consider a body surface point and a vortex frame point that at a given time coincide. Observing that for a generic function, $f = f(\mathbf{x}, t)$,

$$\left. \frac{\partial f}{\partial t} \right|_V = \left. \frac{\partial f}{\partial t} \right|_B + \mathbf{v}_{B-V} \cdot \nabla f$$

where $\partial f / \partial t|_V$ and $\partial f / \partial t|_B$ denote the time derivatives observed, respectively, in the vortex frame and in the body frame, while $\mathbf{v}_{B-V} = \mathbf{v}_V - \mathbf{v}_B$ is the relative velocity between the two frames at the considered point, for $f = \varphi_I^k$ (with φ_I^k denoting the incident potential due to the k th far wake vortex) and recalling that $\dot{\varphi}_I^k = 0$ in the vortex frame, it is possible to obtain, for the time derivative of the incident potential in the body frame,

$$\left. \frac{\partial \varphi_I^k}{\partial t} \right|_B = -\mathbf{v}_{B-V} \cdot \mathbf{u}_I^k \quad (\text{A.4})$$

with \mathbf{u}_I^k known from the (regularized) k th contribution in (8).

If the evaluation of the pressure is carried out within a free-wake solution, each far wake vortex is subject to deformation. In this case, the related (doublet) potential induced in the corresponding vortex frame yields an additional contribution in that it is no longer stationary, although the intensity of the doublet is time independent (indeed, it is given by the potential jump across the wake that is constant following a material point [17, 18]). Nevertheless, this contribution is not taken into account for the vortices that are close to the evaluation point, in that negligible with respect to the contribution from the term in (A.4), due to the very high induced velocity arising. Note that, a further contribution comes from the wake vortices entering the far wake region at each time step, in terms of the corresponding incident potential variation in the unit of time.

A procedure similar to that described above for the evaluation of the $\dot{\varphi}_I^k$ from a wake vortex has been applied in Ref. [37] for the evaluation of the pressure on a body induced by vortex filaments.

Appendix B

This Appendix yields the stiffness matrix appearing in the Fourier-transformed aeroelastic equations, namely (13) and (14).

It is obtained by expressing the stiffness matrix in terms of the Fourier series

$$\mathbf{K}(t) = \mathbf{K}_0 + \sum_{n=1}^N [\mathbf{K}_n^c \cos(\Omega_n t) + \mathbf{K}_n^s \sin(\Omega_n t)]$$

and combining it with the harmonics of \mathbf{q} . The result is that the harmonics of the term $\mathbf{K}(t)\mathbf{q}$ in (12) are given by $\hat{\mathbf{K}}\hat{\mathbf{q}}$ with

$$\hat{\mathbf{K}} = \begin{bmatrix} \mathbf{K}_0 & \frac{1}{2}\mathbf{K}_1^c & \frac{1}{2}\mathbf{K}_1^s & \frac{1}{2}\mathbf{K}_2^c & \frac{1}{2}\mathbf{K}_2^s & \cdots \\ \mathbf{K}_1^c & \mathbf{K}_0 + \frac{1}{2}\mathbf{K}_2^c & \frac{1}{2}\mathbf{K}_2^s & \frac{1}{2}(\mathbf{K}_1^c + \mathbf{K}_3^c) & \frac{1}{2}(\mathbf{K}_1^s + \mathbf{K}_3^s) & \cdots \\ \mathbf{K}_1^s & \frac{1}{2}\mathbf{K}_2^s & \mathbf{K}_0 - \frac{1}{2}\mathbf{K}_2^c & -\frac{1}{2}(\mathbf{K}_1^c - \mathbf{K}_3^c) & \frac{1}{2}(\mathbf{K}_1^s - \mathbf{K}_3^s) & \cdots \\ \mathbf{K}_2^c & \frac{1}{2}(\mathbf{K}_1^c + \mathbf{K}_3^c) & -\frac{1}{2}(\mathbf{K}_1^s - \mathbf{K}_3^s) & \mathbf{K}_0 + \frac{1}{2}\mathbf{K}_4^c & \frac{1}{2}\mathbf{K}_4^s & \cdots \\ \mathbf{K}_2^s & \frac{1}{2}(\mathbf{K}_1^s + \mathbf{K}_3^s) & \frac{1}{2}(\mathbf{K}_1^c - \mathbf{K}_3^c) & \frac{1}{2}\mathbf{K}_4^s & \mathbf{K}_0 - \frac{1}{2}\mathbf{K}_4^c & \cdots \\ \vdots & \vdots & \vdots & \vdots & \vdots & \cdots \end{bmatrix}$$

where only the contribution of the lowest two harmonics is explicitly expressed. Similar expressions are derivable for $\hat{\mathbf{M}}$ and $\hat{\mathbf{C}}$.

References

1. Lim, J.W., Yu, Y.H., Johnson, W.: Calculation of rotor blade-vortex interaction airloads using a multiple-trailer free-wake model. *J. Aircr.* **40**(6), 1123–1130 (2003)

2. Munsky, B., Gandhi, F., Tauszig, L.: An analysis of helicopter blade-vortex interaction noise with flight path or attitude modification. In: 58th Annual Forum of the American Helicopter Society, Montréal, Canada (2002)
3. Liu, L., Patt, D., Friedmann, P.P.: Simultaneous vibration and noise reduction in rotorcraft using aeroelastic simulation. In: 60th Annual Forum of the American Helicopter Society, Baltimore, MD (2004)
4. Patt, D., Liu, L., Friedmann, P.P.: Rotorcraft vibration reduction and noise predictions using a unified aeroelastic response simulation. *J. Am. Helicopter Soc.* **50**(1), 95–106 (2005)
5. Beaumier, P., Delrieux, Y.: Description and validation of the ONERA computational methods for the prediction of blade-vortex interaction noise. *Aerosp. Sci. Technol.* **9**, 31–43 (2005)
6. Datta, A., Chopra, I.: Validation and understanding of UH-60A vibratory loads in steady level flight. *J. Am. Helicopter Soc.* **49**(3), 271–287 (2004)
7. Hansford, R.E., Vorwald, J.: Dynamics workshop on rotor vibratory loads prediction. *J. Am. Helicopter Soc.* **31**(1), 76–87 (1998)
8. Gennaretti, M., Bernardini, G.: Aeroelastic response of helicopter rotors using a 3-D unsteady aerodynamic solver. *Aeronaut. J.* **110**(1114), 793–801 (2006)
9. Gennaretti, M., Molica Colella, M., Bernardini, G.: Analysis of helicopter vibratory hub loads alleviation by cyclic trailing-edge blade flap actuation. *Aeronaut. J.* **113**(1146), 549–556 (2009)
10. Gennaretti, M., Molica Colella, M., Bernardini, G.: Prediction of tiltrotor vibratory loads with inclusion of wing-proprotor aerodynamic interaction. *J. Aircr.* **47**(1), 71–79 (2010)
11. Gennaretti, M., Bernardini, G.: Novel boundary integral formulation for blade-vortex interaction aerodynamics of helicopter rotors. *AIAA J.* **45**(6), 1169–1176 (2007)
12. Gennaretti, M., Corbelli, A., Mastroddi, F.: A comparison among some aeroelastic models for the stability analysis of a flap-lag-torsion helicopter rotor in hover. In: 26th European Rotorcraft Forum, The Hague, The Netherlands, Sept. (2000)
13. Gennaretti, M., Greco, L.: Time-dependent coefficient reduced-order model for unsteady aerodynamics of proprotors. *J. Aircr.* **42**(1), 138–147 (2005)
14. Gennaretti, M., Greco, L.: Whirl flutter analysis of prop-rotors using unsteady aerodynamics reduced-order models. *Aeronaut. J.* **112**(1131), 233–242 (2008)
15. Gennaretti, M., Greco, L.: A multiblade aerodynamic reduced-order model for aeroelastic analysis of helicopter rotors in forward flight. In: 35th European Rotorcraft Forum, Paris, France, Sept. (2010)
16. Bernardini, G., Serafini, J., Ianniello, S., Gennaretti, M.: Assessment of computational models for the effect of aeroelasticity on BVI noise prediction. *Int. J. Aeroacoust.* **6**(3), 199–222 (2007)
17. Morino, L.: A general theory of unsteady compressible potential aerodynamics. NASA CR-2464 (1974)
18. Morino, L., Gennaretti, M.: Boundary integral equation methods for aerodynamics. In: Atluri, S.N. (ed.) *Computational Nonlinear Mechanics in Aerospace Engineering*. Progress in Astronautics & Aeronautics, vol. 146, pp. 279–320. AIAA, New York (1992)
19. Hodges, D.H., Dowell, E.H.: Nonlinear equation for the elastic bending and torsion of twisted nonuniform rotor blades. NASA TN D-7818, December (1974)
20. Hodges, D.H., Ormiston, R.A.: Stability of elastic bending and torsion of uniform cantilever rotor blades in hover with variable structural coupling. NASA TN D-8192, April (1976)
21. Morino, L., Bharadvaj, B.K.: A unified approach for the potential and viscous free-wake analysis of helicopter rotors. *Vertica* **12**, 147–154 (1988)
22. Leishman, J.G.: *Principles of Helicopter Aerodynamics*. Cambridge University Press, Cambridge (2000)
23. Greenberg, J.M.: Airfoil in sinusoidal motion in a pulsating stream. NACA TN-1326, June (1947)
24. Theodorsen, T.: General theory of aerodynamic instability and the mechanism of flutter. NACA report 496 (1935)
25. Van der Wall, B., Leishman, J.G.: The influence of variable flow velocity on unsteady airfoil behavior. *J. Am. Helicopter Soc.* **39**(4), 288–297 (1994)

26. Loewy, R.G.: A two-dimensional approximation of unsteady aerodynamics of rotary wings. *J. Aeronaut. Sci.* **24**(2), 81–92 (1957)
27. Venkatesan, C., Friedmann, P.P.: New approach to finite-state modeling of unsteady aerodynamics. *AIAA J.* **24**(12), 1889–1897 (1986)
28. Gaonkar, G.H., Peters, D.A.: Review of dynamic inflow modeling for rotorcraft flight dynamics. *Vertica* **12**(3), 213–242 (1988)
29. Peters, D.A., He, C.J.: Finite-state induced flow models, part II: three-dimensional rotor disk. *J. Aircr.* **32**(2), 323–333 (1995)
30. Peters, D.A.: How dynamic inflow survives in the competitive world of rotorcraft aerodynamics. *J. Am. Helicopter Soc.* **54**(1), 1–15 (2009)
31. Ffowcs Williams, J.E., Hawkings, D.L.: Sound generated by turbulence and surfaces in arbitrary motion. *Philos. Trans. R. Soc. Lond. A* **264**, 321–342 (1969)
32. Brentner, K.S.: Prediction of helicopter discrete frequency rotor noise—a computer program incorporating realistic blade motions and advanced acoustic formulation. NASA TM-87721 (1986)
33. Farassat, F.: Derivation of formulations 1 and 1A of Farassat. NASA TM-2007-214853 (2007) available at <http://ntrs.nasa.gov>
34. Zhang, J.: Active-passive hybrid optimization of rotor blades with trailing edge flaps. PhD thesis, Department of Aerospace Engineering, The Pennsylvania State University (2001)
35. Bir, G., Chopra, I., et al.: University of Maryland advanced rotor code (UMARC) theory manual. Technical report UM-AERO 94-18, Center for Rotorcraft Education and Research, University of Maryland, College Park, Maryland (1994)
36. Schultz, K.J., Spletstoesser, W., Junker, B., Wagner, W., Schoell, E., Arnaud, G., Mercker, E., Pengel, K., Fertis, D.: A parametric wind tunnel test on rotorcraft aerodynamics and aeroacoustics (HELISHAPE)—test documentation and representative results. In: 22nd European Rotorcraft Forum, Brighton, UK, Sept. (1996)
37. Bi, N.-P., Leishman, J.G., Crouse, G.L.: Investigation of rotor tip vortex interactions with a body. *J. Aircr.* **30**(6), 879–889 (1993)

Variational Analysis and Aerospace Engineering:
Mathematical Challenges for Aerospace Design
Contributions from a Workshop held at the School of
Mathematics in Erice, Italy
Buttazzo, G.; Frediani, A. (Eds.)
2012, XIV, 462 p., Hardcover
ISBN: 978-1-4614-2434-5